Korean J. Chem. Eng., 37(11), 1829-1835 (2020)
DOI: 10.1007/s11814-020-0607-1

pISSN: 0256-1115
eISSN: 1975-7220

Optimizing conical nozzle of venturi ejector in ejector loop reactor using computational fluid dynamics

Enle Xu*,, Xiaofeng Jiang*,**,†, and Long Ding*****

*School of Chemical Engineering and Technology, China University of Mining and Technology, Xuzhou, Jiangsu, 221116, P. R. China
**Chinese National Engineering Research Center of Coal Preparation and Purification, China University of Mining and Technology, Xuzhou 221116, Jiangsu, China
***Weihai New Era Chemical Machinery Co., LTD, Weihai 264200, P. R. China
(*Received 23 January 2020 • Revised 19 May 2020 • Accepted 8 June 2020*)

Abstract−The structure of a conical nozzle is critical to the gas induction of a venturi ejector. In this work, the effect of nozzle structure on the gas induction was investigated by means of multiphase CFD and validating experiments. Under different structures, the maximal gas induction was obtained through analyzing the nozzle outlet velocity (NOV), nozzle inlet velocity (NIV), as well as nozzle shrinking angle (NSA). The simulated inlet pressure is positively proportional to inlet flow rate, which is in good agreement with experimental results. The simulated results reveal that the inlet pressure and gas induction increase with the increasing NOV. Considering the operational characteristics of centrifugal pump, the recommended NOV is about 21.8 m/s. NIV and NSA show little impact on gas induction and inlet pressure. Based on the pipeline energy consumption, the recommended NIV is the same as the outlet velocity of centrifugal pump. The recommended NSA is about 20° to obtain the maximal gas induction.

Keywords: Conical Nozzle, Gas Induction, Nozzle Outlet Velocity, Nozzle Shrinking Angle, Nozzle Inlet Velocity

INTRODUCTION

Effective dispersion between gas phase and liquid phase is important in the chemical industry, such as multiphase reactions [1-3]. An ejector loop reactor (ELR) is more and more appreciated as a typical multiphase mixed reactor [4-7]. Fig. 1 provides a schematic diagram of the ELR, which mainly consists of recycling pump, venturi ejector, heater exchanger and vessel. The gas phase is introduced into the venturi ejector by the high speed liquid from the recycling pump. The mixing behavior of gas and liquid phases occurs in the venturi ejector and vessel. The recycling pump provides all the power for this system. Compared to the stirred tank reactor [8-11], ELR exhibits high efficiency of heat and mass transfer due to the heat exchanger and recycling pump. Furthermore, ELR is preferred for a high pressure reaction and the easy scale-up ability with the advantage of being without rotating parts.

It is proved that ELR is of great potential for different chemical reactions. Poissonnier et al. [12] performed bimodal reaction in ELR and obtained higher homogeneous product yields with a low catalyst-to-liquid ratio. Serio et al. [13] studied ethoxylation reactions in different reactor types and pointed out that ELR can achieve maximum productivity under a low power input. Warmeling et al. [14] demonstrated that ELR could enhance catalytic reactions.

The venturi ejector is the key part to determine the performance of the ELR. Fig. 2 presents a schematic diagram of the venturi ejector. The key components of the venturi ejector are the conical nozzle, suction chamber, mixing tube and diffuser. The liquid from the recycling pump is accelerated in the conical nozzle. According to Bernoulli's theorem, the static pressure drop generates a vacuuming effect at the nozzle outlet. The gas is drawn into the suction chamber by the pressure difference. The dispersion between liquid

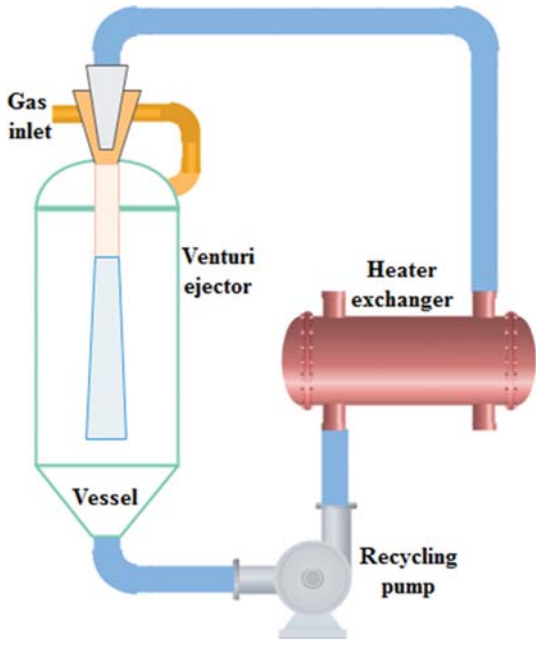

Fig. 1. Schematic diagram of ELR.

†To whom correspondence should be addressed.
E-mail: xiaofeng.jiang@cumt.edu.cn

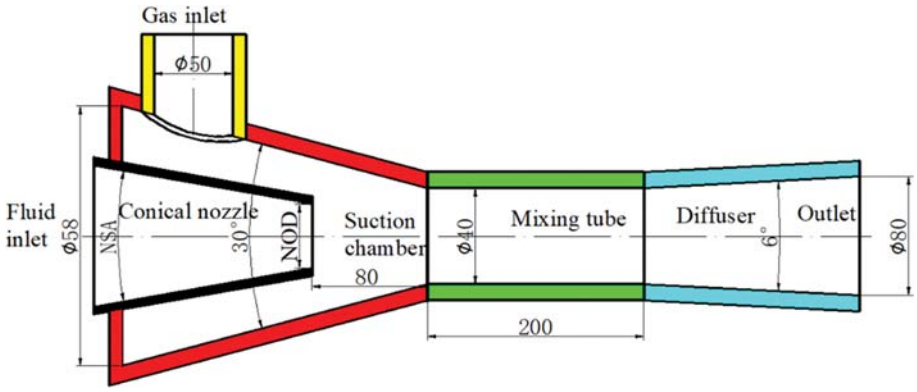

Fig. 2. Schematic diagram of the venturi ejector structure.

and gas happens in the mixing tube. When the velocity of the liquid-gas mixture in the diffuser is reduced, the static pressure increases.

The entrainment ratio, given by the ratio of gas induction to liquid flow rate, is the critical parameter to influence the bubble size distribution, the hydrodynamics and mass transfer properties of ELR [15,16]. Some approaches have been suggested to improve the entrainment ratio. Sharma et al. [17] found that mixing tube length and nozzle diameter have a more complex impact on gas induction. Kim et al. [18] designed a water-driven annular type ejector loop for air absorption and found that entrained air flow rate had a linear relationship with water flow rate. Song et al. [19] concluded that simple change of nozzle shape can greatly improve the ejector performance under high back pressure conditions. Sharma et al. [20] studied the effect of turbulence on the jet dynamics and gas induction rate in an ejector. Zhang et al. [21] investigated the effect of nozzle position on entrainment ratio and obtained the optimal nozzle position of 6 mm for a given operating conditions and fixed geometries. Chen et al. [22] proposed an ejector with bypass to improve the entrainment ratio and investigated the effects of operational and bypass geometrical factors on the ejector entrained capacity.

ELR structure, especially the conical nozzle, is one of the main factors to determine the vacuuming effect and the entrainment ratio. Though some investigations focused on the optimized nozzle, the universal conclusion about the nozzle design scheme considering the operational characteristics of ELR has not yet been fully understood. The nozzle has a close relation with the recycling pump, especially the centrifugal pump, because the nozzle inlet pressure changes according to the nozzle outlet velocity (NOV), which will affect the operating status of the recycling pump as well as the nozzle inlet flow rate. The universal design parameter of nozzle structure could be obtained if nozzle inlet velocity (NIV), NOV and nozzle shrinking angle (NSA) were confirmed. Thus, this paper aimed to optimize the nozzle structure for the purpose of the maximal gas induction considering the characteristic of the recycling pump by means of the multiphase CFD and validating experiments, and to establish the universal nozzle velocity and angle.

EXPERIMENTS

The experimental setup and flow diagram of a simple ELR is given in Fig. 3. Water and air were the experimental liquid and gas, respectively. The centrifugal pump was chosen as the recycling pump with the rated flow rate of 15 m^3/h and the rated lift of 30 m. A frequency converter was installed for the centrifugal pump which could adjust the water flow rate. A pressure transducer and flow transducer were utilized to quantify the pressure and flow rate of the liquid into the venturi ejector with a precision of ±0.5% preset in the pipes.

The dimension of the experimental venturi ejector is partially shown in Fig. 2. Because the liquid-gas mixture from the venturi ejector enters into a tank under the atmospheric pressure, the outlet pressure of venturi ejector is equal to the atmospheric pressure.

MODELING APPROACH

1. Geometries and Grids

In this paper, some different models were developed to optimize the nozzle structure. The nozzle outlet diameter (NOD), NIV and NSA with different dimensions are presented in Table 1. The dimen-

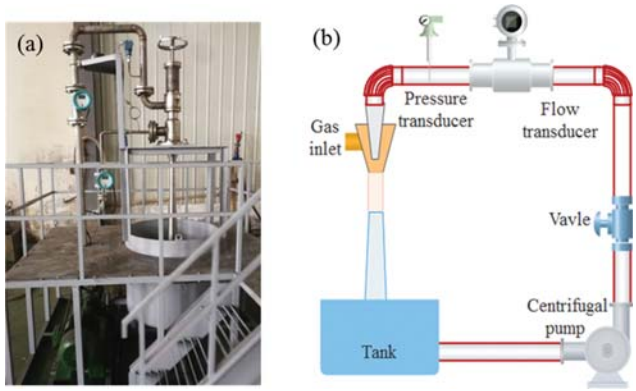

Fig. 3. Experimental setup and flow diagram.

Table 1. Simulation models with different dimensions

NOD mm				NIV m/s				NSA				
13	14	16	18	1.0	2.0	3.0	4.0	8°	16°	20°	24°	28°

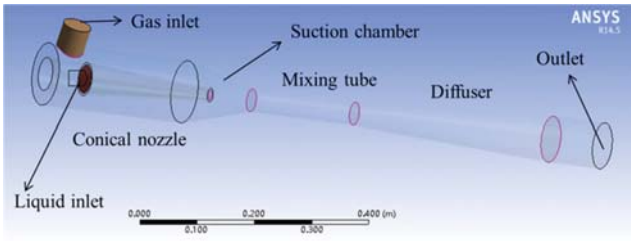

Fig. 4. Geometry model.

sions of the venturi ejector structure in simulation are the same as the experimental setup. Fig. 4 exhibits the geometry model generated in the preprocessor ANSYS Workbench Design Modeler 14.5.

The mesh model was produced in the ICEM 14.5. The O-grid block was chosen as the grid topology to produce the structured mesh. The global mesh size was used to control the grid distribution. The first cell height was about 0.4 mm at the position of nozzle outlet. The quality of the meshes was analyzed using the orthogonal quality. The minimum orthogonal quality was 0.67, indicating that the mesh was fair. The grid distributions of the center plane and outlet surface were preset in Fig. 5(a) and (b), respectively.

2. Mixture Model and Governing Equation

The mixture model is a simplified multiphase model that can be used to depict multiphase flows where the phases move at different velocities. It can perform as well as a full Eulerian multiphase model for bubbly flows, which is in accord with the venturi ejector. The mixture model can model n phases by solving the momentum and continuity equations for the mixture.

The continuity equation for the mixture is

$$\nabla \bullet (\rho_m \mathrm{u}_m) = 0 \tag{1}$$

where ρ_m is the mixture density

$$\rho_m = \sum_{k=1}^{n} \alpha_k \rho_k \tag{2}$$

and u_m is the mass-averaged velocity

$$\mathrm{u}_m = \frac{\sum_{k=1}^{n} \alpha_k \rho_k \mathrm{u}_k}{\rho_m} \tag{3}$$

α_k, ρ_k and u_k is the volume fraction, density and velocity of phase k, respectively; t is the time; n is the number of phases where n=2 is for this simulation model.

The momentum equation for the mixture could be obtained by summing the individual momentum equations of all phases. It can be expressed as

$$\nabla \bullet (\rho_m \mathrm{u}_m \mathrm{u}_m) = -\nabla \mathrm{p} + \nabla \bullet [\mu_m (\nabla \mathrm{u}_m + \nabla \mathrm{u}_m^T)] + \mathrm{F} + \nabla \bullet \left(\sum_{k=1}^{n} \alpha_k \rho_k \mathrm{u}_{d,k} \mathrm{u}_{d,k} \right) \tag{4}$$

where F is a body force, and μ_m is the viscosity of the mixture:

$$\mu_m = \sum_{k=1}^{n} \alpha_k \mu_k \tag{5}$$

$\mathrm{u}_{d,k}$ is the drift velocity for phase k:

$$\mathrm{u}_{d,k} = \mathrm{u}_k - \mathrm{u}_m \tag{6}$$

Among the standard k-ε models, the RNG k-ε model, and realizable k-ε model, one of the major documented drawbacks of the standard k-ε model is the over-prediction of turbulent viscosity at lower Reynolds numbers (Re<10,000). However, in a practical situation, the Reynolds number is very high (Re>115,444) [23,24]. Considering the robustness, economy, and reasonable accuracy for a wide range of turbulent flows, the standard k-ε model was selected to study the venturi ejector [25-28]. The turbulent viscosity, μ_t, was calculated based on model transport equations for the turbulence kinetic energy (k) and its dissipation rate (ε). The k, ε and μ_t were obtained from the following transport equations:

$$\frac{\partial (\rho_m \mathrm{k} \mathrm{u}_m)}{\partial \mathrm{x}_i} = \frac{\partial}{\partial \mathrm{x}_j} \left[\left(\mu_m + \frac{\mu_t}{\sigma_k} \right) \frac{\partial \mathrm{k}}{\partial \mathrm{x}_j} \right] + \mathrm{G}_k - \rho_m \varepsilon \tag{7}$$

$$\frac{\partial (\rho_m \varepsilon \mathrm{u}_m)}{\partial \mathrm{x}_i} = \frac{\partial}{\partial \mathrm{x}_j} \left[\left(\mu_m + \frac{\mu_t}{\sigma_\varepsilon} \right) \frac{\partial \varepsilon}{\partial \mathrm{x}_j} \right] + \mathrm{c}_{1\varepsilon} \frac{\varepsilon}{\mathrm{k}} \mathrm{G}_k - \mathrm{c}_{2\varepsilon} \rho_m \frac{\varepsilon^2}{\mathrm{k}} \tag{8}$$

$$\mu_t = \frac{\mathrm{c}_\mu \rho_m \mathrm{k}^2}{\varepsilon} \tag{9}$$

In these equations, G_k represents the generation of turbulence kinetic energy due to the mean velocity gradients, σ_k=1.0, σ_ε=1.3, $\mathrm{C}_{1\varepsilon}$=1.44, $\mathrm{C}_{2\varepsilon}$=1.92, C_μ=0.09.

3. Numerical Simulation Settings

The commercial software ANSYS Fluent 14.5 was used as the CFD solver. The SIMPLE scheme was adopted for pressure-veloc-

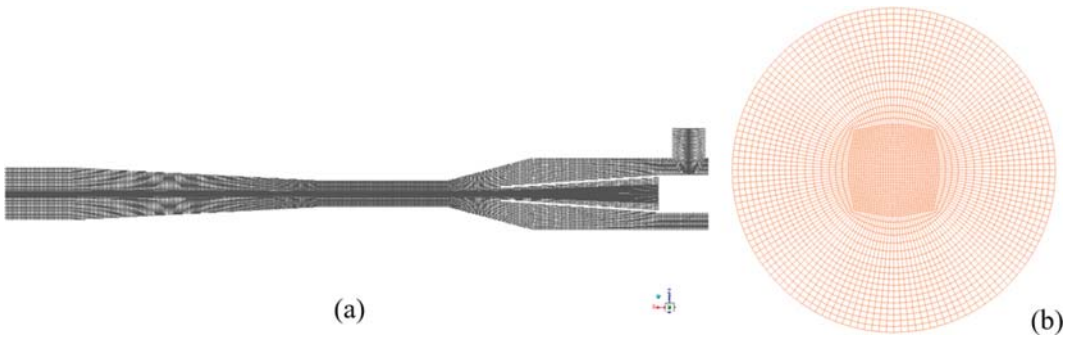

Fig. 5. Grid generation at center plane (a) and outlet (b).

ity coupling. Both the first-order upwind and second-order upwind were tested in this model; however, practically identical results were found. The first-order upwind was chosen for spatial discretization due to the strength of its calculation time for this simulated model [7]. The standard pressure, least squares cell based gradient were employed in this model.

Water was selected as the liquid phase and the air worked as the gas phase. The boundary conditions for liquid inlet, gas inlet and outlet were velocity-inlet, pressure-inlet and pressure-outlet, respectively. The initial condition of simulation model was full of liquid phase. Residuals for governing equations were performed within 1.0×10^{-5} relative error as a criterion for convergence of the solution. The gas induction reached a stable level and the mass flow rate was balanced for entering and leaving the model as another converged condition.

4. Mesh Independence Study and Experiment Validation

To validate CFD simulation accuracy, Fig. 6 presents the effect the mesh number on the gas induction at NIV of 2.0 m/s and NOD of 16 mm. In this paper, gas induction takes the place of entrainment ratio because they have the same change rule when the liquid inlet flow rate keeps unchanged. As the mesh number increases, the gas induction decreases slowly and then keeps at a stable level. When the mesh number increased from 1,855,628 to 2,665,253, the gas induction changed from 0.0112 m^3/s to 0.0111 m^3/s and had little change. Thus, the mesh number used in the simulation was about 1,855,628.

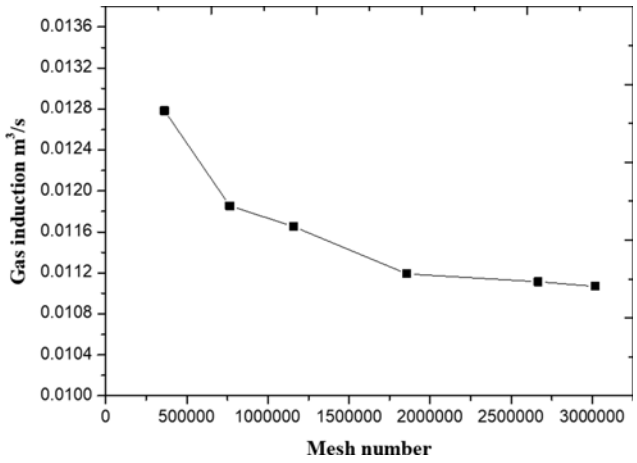

Fig. 6. Relation between gas induction and mesh number.

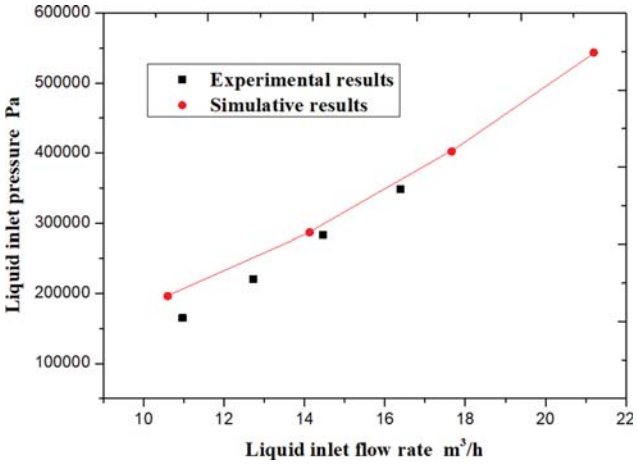

Fig. 7. Comparison simulated results of inlet pressure with test data.

Fig. 7 illustrates the comparison of inlet pressure simulated results with experimental results under different liquid inlet flow rate. The simulated flow rate is determined according to NOV (15.0 m/s, 20.0 m/s, 25.0 m/s, 30.0 m/s), so the range of simulated flow rate changes from 10.6 m^3/h to 21.2 m^3/h. The range of experimental flow rate is determined by the rated flow rate and lift of recycling pump. The maximal flow rate can only reach 16.4 m^3/h for the venturi ejector with NOD of 16.0 mm. Due to the limitation of the experimental setup, the range of the comparison have some inevitable differences. From this figure, it is clear that liquid inlet pressure is proportional to liquid inlet flow rate. In addition, CFD simulated results show the same evolution trend with the experimental inlet pressure, which indicates that CFD simulation is reasonable.

RESULTS AND DISCUSSION

1. Optimizing Nozzle Outlet Velocity

In this part, the NOV changes with NOD under the same liquid inlet flow rate. The value of NIV is 2.0 m/s, the nozzle inlet diameter is 50 mm, the NSA is set to be 8°, and the different values of NOD are shown in Table 1. Fig. 8(a) and (b) present the axial velocity contour of center section, radial velocity contour of different axial distances, respectively. For the sake of comparing the

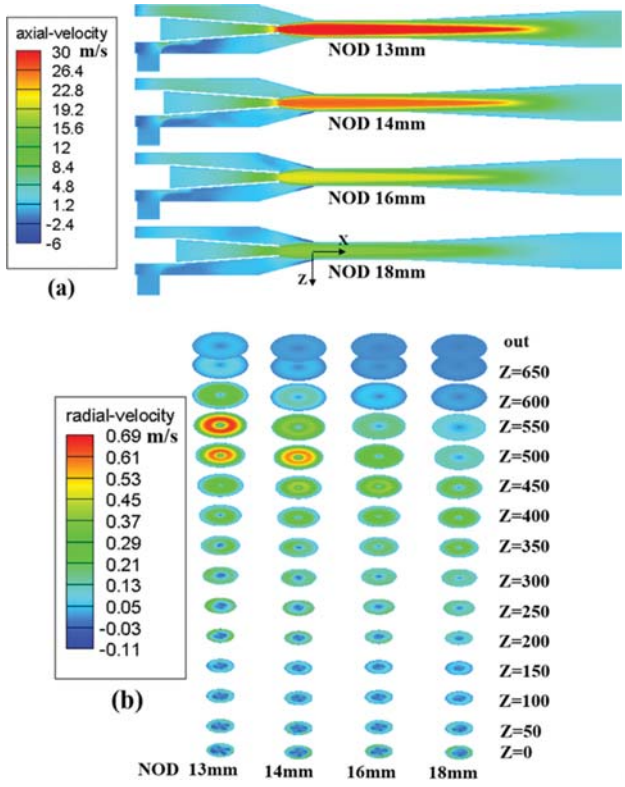

Fig. 8. (a) Axial velocity of center section and (b) radial velocity of different axial distances.

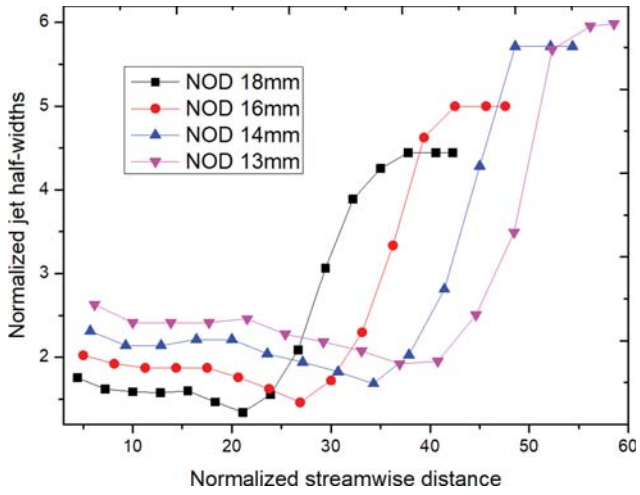

Fig. 9. Normalized jet half-width along normalized streamwise distance for different NOD.

velocity magnitude, the same kind of contour legend is set for different NOD contours. As Fig. 8(a) shown, the liquid axial velocity accelerates gradually due to the decreasing flow area in the conical nozzle. The maximal liquid velocity appears in the position of nozzle outlet, which decreases with the rising NOD. The velocity core zone fades away gradually when the liquid leaves from the nozzle outlet. For this model, the velocity core zone disappears eventually in the diffuser. The velocity core zone vanishes later for smaller NOD due to lager liquid velocity.

The radial velocity reflects the gas-liquid diffusion. From Fig. 8(b), it is clear that the radial velocity is very small in the mixing tube due to the unchanged flow area, indicating that the gas-liquid phase hardly mingles. The gas-liquid diffusion mainly happens in the part of diffuser on account of the increased flow area. When the velocity core region disappears, the radial velocity reaches its maximum. The radial velocity increases with the decrease of NOD because of the increasing liquid velocity.

Fig. 9 shows a comparison of jet half-width from the mixing tube inlet to outlet for different NOD. The jet half-width and streamwise distance are both normalized by NOD. The jet half-width is defined as the transverse distance from the jet axis to the location where the mean axial velocity is half of the centerline value [29]. In jet flow, the velocity gradient generates turbulence. Turbulent eddies cause the entrainment of the surrounding fluid into the jet flow. Thus, the jet half-width could represent the gas induction. According to normalized jet half-width, it could be observed that the gas induction increases with the decreasing NOD. Thus NOV is a critical factor for the gas induction.

Fig. 10 provides volume of fluid (VOF) contour of center section for different NOD. As Fig. 10 shown, the conical nozzle is full of liquid and the suction chamber is filled with air. The gas phase is entrained by liquid into mixing tube together. Due to the increasing of flow area in diffuser, the liquid phase disperses the gas phase gradually until the mixture reaches a homogeneous status. Combined with Fig. 8 and 9, it can be concluded that the mixing behavior between liquid and gas phases will be benefit from larger NOD and less gas induction.

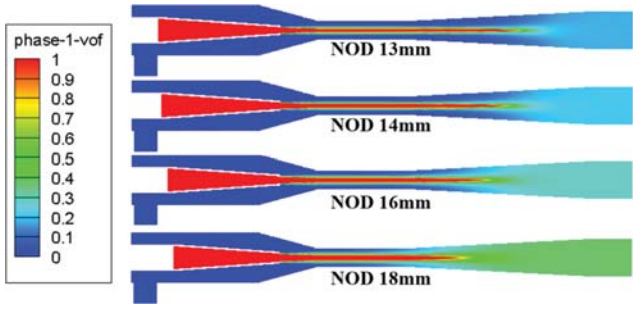

Fig. 10. VOF contour of center section for different NOD.

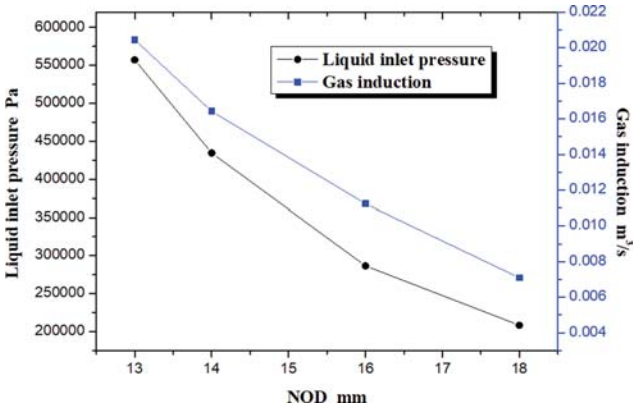

Fig. 11. Relation among liquid inlet pressure, gas induction and NOD.

Fig. 11 provides the relation among liquid inlet pressure, gas induction and NOD. From this figure, the liquid inlet pressure and gas induction decrease with the increasing NOD. The reason is that the smaller NOD will lead to larger NOV at the constant inlet flow rate which needs more input power. In industry, the inlet pressure of venture ejector is always provided through the centrifugal pump. It is difficult to satisfy the rising inlet pressure under the unchanged flow rate. The flow rate will reduce with the increasing of pressure for a specific centrifugal pump which is the operational characteristics of centrifugal pump. Therefore, an optimal NOD

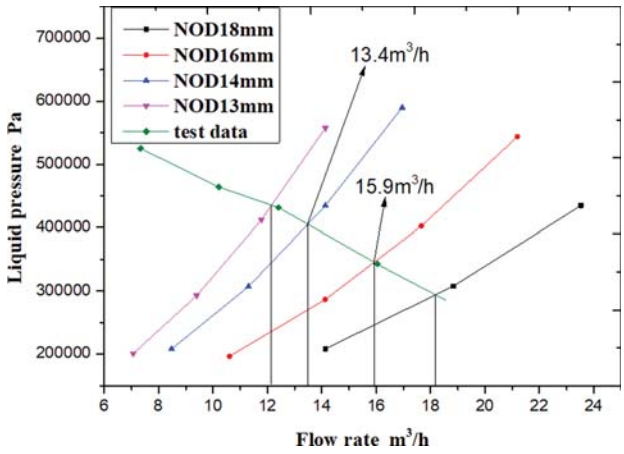

Fig. 12. Relation between liquid pressure and flow rate.

and NOV should exist based on the operation characteristics of centrifugal pump.

Fig. 12 illustrates the relation between liquid pressure and flow rate. Four NOD curves that the liquid inlet pressure increases with the increasing of inlet flow rate were obtained through CFD simulation. Another test data was acquired through measuring the outlet pressure of the experimental centrifugal pump. The pressure decreases with the increasing flow rate, which is corresponding to the centrifugal pump characteristic curve. A series of intersection points can be obtained by simulated NOD curves and test date curve. Each intersection point correlates an inlet flow rate for the venturi ejector when the centrifugal pump and the specific NOD are used together. Combined with each intersection point and the relation between gas induction and inlet flow rate, the gas induction can be obtained for specific NOD which is shown in Fig. 13. From Fig. 13, gas induction increases first and then remains stable with the reducing NOD. For the purpose of maximal gas induction, the optimal NOD is 16 mm. The recommended NOV can be calculated as about 21.8 m/s, according to the inlet flow rate and NOD.

2. Optimizing Nozzle Inlet Velocity

In this part, NIV changes according to nozzle inlet diameter under the same liquid inlet flow rate. The NSA is 16°, NOD is 16 mm, and the different values of NIV are shown in Table 1. Fig. 14 shows the center line velocity and VOF for different NIV. The center line velocity and VOF is in accord with velocity contour of Fig. 8(a) and VOF contour of Fig. 10, respectively. From Fig. 14, it is clear that NIV has no influence on the internal flow field since nozzle out velocity has no change with NIV.

Fig. 15 provides the relation among gas induction, liquid inlet pressure and NIV. The variation range of gas induction is only 0.0003 m^3/s while NIV changes from 1.0 m/s to 4.0 m/s. Therefore, NIV has a negligible influence on gas induction. The liquid inlet pressure decreases with the increasing NIV. In fact, NIV is on behalf of kinetic energy input the venturi ejector. The requisite static pressure, liquid inlet pressure, will reduce when the kinetic energy increases with the rising NIV. Though the high NIV would reduce the inlet pressure, the high velocity in pipeline will augment the energy consumption. For overall consideration, the recommended NIV should be equal to the outlet velocity of centrifugal pump.

3. Optimizing Nozzle Shrinking Angle

To optimize NSA, NIV of 2.0 m/s, nozzle inlet diameter of 50 mm and NOD of 16 mm remain unchanged. The different values of NSA are given in Table 1. Fig. 16 shows the center line velocity of venturi ejector for different NSA. The nozzle length shortens

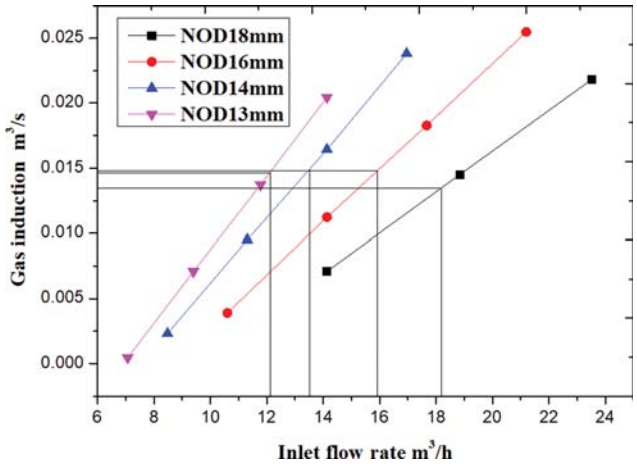

Fig. 13. Relation between gas induction and inlet flow rate.

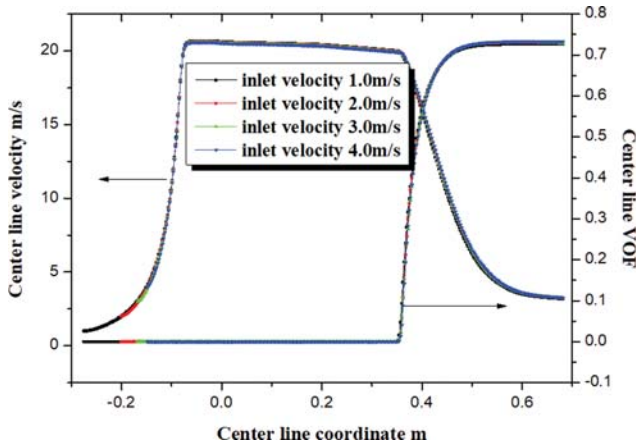

Fig. 14. Center line velocity and VOF for different NIV.

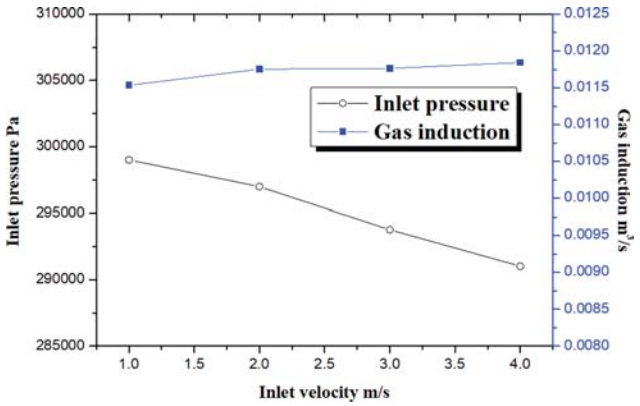

Fig. 15. Relation among gas induction, inlet pressure and NIV.

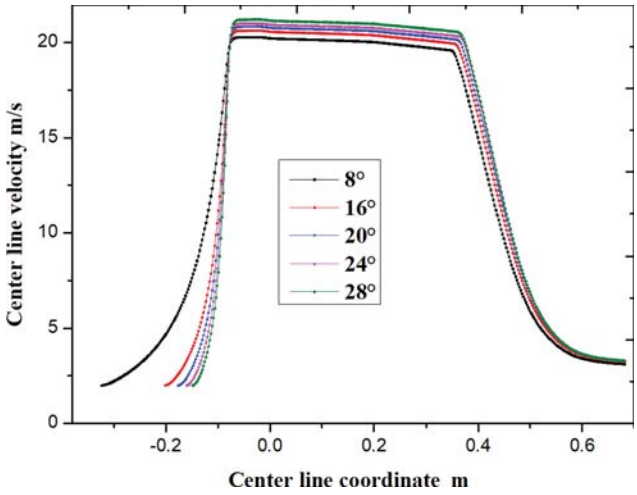

Fig. 16. Center line velocity for different NSA.

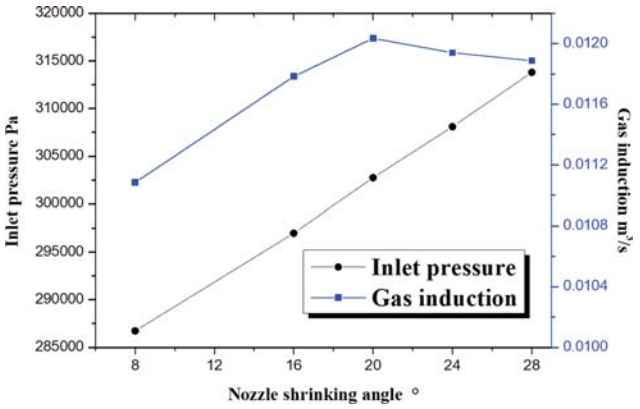

Fig. 17. Relation among gas induction, inlet pressure and NSA.

with the rising NSA, which causes a sharp change of velocity. This may be the reason that the maximal velocity increases with the reducing of NSA, which can be found from Fig. 16.

Fig. 17 describes the relation among gas induction, inlet pressure and NSA. When NSA changes from 8° to 20°, the increasing amplitude of gas induction and inlet pressure is only 8.3% and 6.4%, respectively, which shows that the NSA has little impact on the performance of venturi ejector. However, gas induction increases to maximum first and then decreases gradually with the increasing NSA. The increasing NSA leads to more fluid energy loss and rising inlet pressure, which directly influences the gas induction. Based on the simulated results, the recommended NSA is about 20° for the maximal gas induction.

CONCLUSION

The conical nozzle structure is critical to the gas induction of venturi ejector which directly affects the ELR performance. The nozzle structure was designed as the values of NIV, NOV and NSA are confirmed. To obtain the universal design scheme for a conical nozzle, the nozzle structure was optimized considering the operational characteristics of a centrifugal pump by means of CFD modeling and validating experiments. The simulated inlet pressure shows the same trend with the experimental inlet pressure, indicating that CFD simulation is reasonable.

Based on the simulation results, the inlet pressure and gas induction decrease with the increasing NOD. Considering the centrifugal pump efficiency, the recommended NOV is about 21.8 m/s. NIV shows a negligible influence on gas induction. Inlet pressure decreases with the increasing NIV. Considering the pipeline energy consumption, the recommended NIV is equal to the outlet velocity of centrifugal pump. Gas induction increases to maximum first, and then decreases gradually with the increase of NSA. The recommended NSA is about 20°. This research confirmed the optimal NIV, NOV and NSA for the maximal gas induction which provides theoretic guidance to design high-efficient conical nozzle.

ACKNOWLEDGEMENTS

This research was supported by the Fundamental Research Funds for the Central Universities (2020QN51).

REFERENCES

1. Y. Gao, X. Gao, D. Hong, Y. Cheng, L. Wang and X. Li, *AIChE J.*, **65**, 16537 (2019).
2. J. Poissonnier, J. W. Thybaut and G. B. Marin, *AIChE J.*, **63**, 111 (2017).
3. Q. Chu, P. Wang, G. He, M. Li, H. Zhu, R. Liu and F. Pei, *Chem. Eng. J.*, **325**, 169 (2017).
4. Z. Khan and J. B. Joshi, *Chem. Eng. Sci.*, **127**, 323 (2015).
5. W. Ludwig, R. G. Szafran, A. Kmiec and J. Dziak, *Pro. Eng.*, **42**, 1157 (2012).
6. C. S. Mathpati, S. S. Deshpande and J. B. Joshi, *AIChE J.*, **55**, 2526 (2009).
7. Y. Gao, D. Hong, Y. Cheng, L. Wang and X. Li, *Chem. Eng. Res. Des.*, **141**, 66 (2019).
8. S. Weber, S. Schaepe, S. Freyer, M.-H. Kopf and C. Dietzsch, *Chem. Eng. Process.*, **131**, 43 (2018).
9. L. L. V. Dierendonck, *Ind. Eng. Chem. Res.*, **37**, 734 (1998).
10. J. Esteban, H. Warmeling and A. J. Vorholt, *Chem. Ing. Tech.*, **91**, 560 (2019).
11. H. Warmeling, D. Janz, M. Peters and A. J. Vorholt, *Chem. Eng. J.*, **330**, 585 (2017).
12. J. Poissonnier, J. W. Thybaut and G. B. Marin, *Ind. Eng. Chem. Res.*, **56**, 14192 (2017).
13. M. Di Serio, R. Tesser and E. Santacesaria, *Ind. Eng. Chem. Res.*, **44**, 9482 (2005).
14. H. Warmeling, A. Behr and A. J. Vorholt, *Chem. Eng. Sci.*, **149**, 229 (2016).
15. G. M. Evans, A. K. Biń and P. M. Machniewski, *Chem. Eng. Sci.*, **56**, 1151 (2001).
16. P. Havelka, V. Linek, J. Sinkule, J. Zahradnik and M. Fialova, *Chem. Eng. Sci.*, **55**, 535 (2000).
17. D. V. Sharma, A. W. Patwardhan and V. V. Ranade, *Chem. Eng. Res. Des.*, **125**, 24 (2017).
18. Y. K. Kim, D. Y. Lee, H. D. Kim, J. H. Ahn and K. C. Kim, *J. Mech. Sci. Technol.*, **26**, 2773 (2012).
19. X. Song, M. Cao, W. Shin, W. Cao, S. Kang and Y. Park, *Math. Probl. Eng.*, **2014**, 1 (2014).
20. D. Sharma, A. Patwardhan and V. Ranade, *Energy*, **164**, 10 (2018).
21. K. Zhang, X. Zhu, X. Ren, Q. Qiu and S. Shen, *Appl. Therm. Eng.*, **126**, 594 (2017).
22. W. Chen, H. Chen, C. Shi, K. Xue, D. Chong and J. Yan, *Appl. Therm. Eng.*, **99**, 476 (2016).
23. C. Li, Y. Li and L. Wang, *Appl. Therm. Eng.*, **48**, 237 (2012).
24. C. Li and Y. Z. Li, *Chem. Eng. Sci.*, **66**, 405 (2011).
25. E. Bumrungthaichaichan, *Korean J. Chem. Eng.*, **33**, 3050 (2016).
26. G. Yuan, L. Zhang, H. Zhang and Z. Wang, *Desalination*, **276**, 89 (2011).
27. M. T. Kandakure, V. G. Gaikar and A. W. Patwardhan, *Chem. Eng. Sci.*, **60**, 6391 (2005).
28. P. Zheng, B. Li and J. Qin, *Energy*, **155**, 1129 (2018).
29. G. Singh, T. Sundararajan and K. A. Bhaskaran, *J. Fluids Eng.*, **125**, 652 (2003).